Silica-supported, narrowly distributed, subnanometric Pt-Zn particles from single sites with high propane dehydrogenation performance

Author(s):
Rochlitz, Lukas; Searles, Keith; Alfke, Jan; Zemlyanov, Dmitry; Safonova, Olga V.; Copéret, Christophe

Publication date:
2020-02-14

Permanent link:
https://doi.org/10.3929/ethz-b-000401882

Originally published in:
Chemical Science 11(6), https://doi.org/10.1039/c9sc05599a

Chemical Science

ROYAL SOCIETY OF CHEMISTRY

EDGE ARTICLE

View Article Online
View Journal | View Issue

Cite this: *Chem. Sci.*, 2020, **11**, 1549

All publication charges for this article have been paid for by the Royal Society of Chemistry

Received 5th November 2019
Accepted 20th December 2019

DOI: 10.1039/c9sc05599a

rsc.li/chemical-science

Silica-supported, narrowly distributed, subnanometric Pt–Zn particles from single sites with high propane dehydrogenation performance†

Lukas Rochlitz,[a] Keith Searles,[a] Jan Alfke,[ac] Dmitry Zemlyanov,[b] Olga V. Safonova[c] and Christophe Copéret *[a]

The development of highly productive, selective and stable propane dehydrogenation catalysts for propene production is strategic due to the increasing need for propene and the availability of shale gas, an abundant source of light alkanes. In that context, the combination of surface organometallic chemistry (SOMC) and a thermolytic molecular precursor (TMP) approach is used to prepare bimetallic subnanometric and narrowly distributed Pt–Zn alloyed particles supported on silica *via* grafting of a Pt precursor on surface OH groups present in a Zn single-site containing material followed by a H_2 reduction treatment. This material, that exhibits a Zn to Pt molar ratio of 3 : 2 in the form of alloyed Pt–Zn particles with a 0.2 to 0.4 fraction of the overall Zn amount remaining as Zn^{II} sites on the silica surface, catalyzes propane dehydrogenation (PDH) with high productivity (703 $g_{C_3H_6}$ g_{Pt}^{-1} h^{-1} to 375 $g_{C_3H_6}$ g_{Pt}^{-1} h^{-1}) and very low deactivation rates (k_d = 0.027 h^{-1}) over 30 h at high WHSV (75 h^{-1}). This study demonstrates how SOMC can provide access to highly efficient and tailored catalysts through the stepwise introduction of specific elements *via* grafting to generate small, homogeneously and narrowly distributed supported alloyed nanoparticles at controlled interfaces.

Introduction

Propene is the second most utilized building block of the petrochemical industry besides ethene, and its production has been dramatically influenced by the emergence of shale gas resources. Indeed, crackers have been converted from naphtha to ethane units, with ethane feedstocks predominantly producing ethene, thereby reducing propene production. To compensate for the resulting propene production gap, the development of on-purpose propene production technologies has thus been on the rise.[1,2] The most used on-purpose technology is selective propane dehydrogenation (PDH), a highly energy intensive process (ΔH^0_{298} = 124.3 kJ mol^{-1}), industrially implemented mainly *via* two processes using a bimetallic Pt–Sn/Al_2O_3 (UOP Oleflex process) or a metal-oxide based Cr_2O_3/Al_2O_3 (Lummus Catofin process) catalyst.[3] Due to the requirement of high reaction temperatures (500–700 °C) to reach reasonable conversion levels, one of the biggest issues for the existing systems is catalyst stability due to coke formation and sintering requiring constant and rapid regeneration.[3] The development and understanding of catalytic systems with increased stability while keeping a high selectivity and productivity is thus an intense field of research. In particular, major research endeavors focused on bi- and multi-metallic systems related to the industrial Pt–Sn/Al_2O_3 catalyst. In all cases, a combination of Pt with a second metal (In, Sn, Ga, Cu, Zn, *etc.*) beneficially influenced the catalyst performance as compared to monometallic Pt catalysts.[4–9] While the selectivity for most of the systems reaches high levels, all of them suffer from deactivation. Zn, a highly abundant and non-toxic metal, is of special interest as the second component in bimetallic systems for PDH but has been studied less extensively when compared to more prominent post-transition-metals Sn and Ga.[3,10]

Most synthetic strategies for bimetallic Pt–Zn dehydrogenation catalysts rely on well-established impregnation techniques.[9,11,12] While being simple catalyst preparation methods, impregnation techniques typically yield poorly defined systems with inhomogeneous distribution of the components due to complex dissolution/precipitation events that occur in aqueous conditions. In order to develop more controlled preparation methods, surface organometallic chemistry (SOMC)[13–15] in combination with the thermolytic molecular precursor approach (TMP)[16,17] has emerged as a powerful preparation technique. In particular, it has been shown that supported single-sites can be used as building blocks to generate

[a]*Department of Chemistry and Applied Biosciences, ETH Zürich, Vladimir-Prelog-Weg 1-5, CH-8093 Zürich, Switzerland. E-mail: ccoperet@ethz.ch*

[b]*Birck Nanotechnology Center, Purdue University, 1205 West State Street, West Lafayette, Indiana 47907, USA*

[c]*Paul Scherrer Institut, CH-5232 Villigen, Switzerland*

† Electronic supplementary information (ESI) available: Experimental details, material characterization data, catalytic measurement details. See DOI: 10.1039/c9sc05599a

supported nanoparticles with controlled interfaces, allowing the introduction of dopants at the interface between silica and the metal particles or alternatively yielding a bimetallic alloy supported on SiO_2.[17–20] A Pt–Ga alloy prepared through this approach displays high productivity and stability in the PDH reaction that has been attributed to surface dilution of Pt upon the introduction of gallium.[21]

In view of the known activity of Pt–Zn in PDH and improved performance of catalysts prepared *via* SOMC/TMP approach, we reason that SOMC could constitute an ideal way to generate small and narrowly dispersed Pt–Zn alloys by first installing Zn^{II} single sites on a SiO_2 support followed by anchoring of a Pt precursor on the **Zn^{II}/SiO_2** material and a subsequent treatment under H_2 to generate the desired particles. These silica-supported Pt–Zn nanoparticles were characterized by a multi-technique approach (CO and pyridine adsorption FTIR as well as X-ray photoelectron spectroscopy (XPS) and X-ray absorption spectroscopy (XAS) studies); they show high productivity (703 $g_{C_3H_6}/(g_{Pt}^{-1}\ h^{-1})$), high selectivity (≥95%) and an outstanding stability ($k_d = 0.027$) at high WHSV compared to other Pt–Zn based systems for PDH at 550 °C. This improved performance is attributed to the formation of subnanometric and narrowly distributed alloyed particles supported on Zn^{II} modified silica that likely plays a role in stabilizing these particles under PDH reaction conditions.

Results and discussion

The bimetallic Pt–Zn system was prepared *via* SOMC in a three-step process involving first the generation of Zn single-sites, then grafting of Pt(II) molecular precursor onto regenerated OH groups followed by a hydrogen treatment. Grafting of $[Zn(OSi(OtBu)_3)_2]_2$ on SiO_{2-700} followed by a thermal treatment at 600 °C yielded **Zn^{II}/SiO_2** as a white solid that contains Zn^{II} single sites (1.73 wt% Zn to 0.80 Zn per nm^2), free of organic ligands along with isolated OH sites (0.66 OH per nm^2) (Fig. 1(a)).[22,23] In the next step, $[Pt(OSi(OtBu)_3)_2(COD)]$ (1.2 equiv./OH)[24,25] (COD = 1,5-cyclooctadiene) was grafted onto the surface OH groups of **Zn^{II}/SiO_2**; the resulting supernatant contained $[Pt(OSi(OtBu)_3)_2(COD)]$ (0.35 equiv. Pt_{added}^{-1}) and $HOSi(OtBu)_3$ (0.35 equiv. Pt_{added}^{-1}). The obtained white material – **$Pt(OSi(OtBu)_3)(COD)Zn^{II}/SiO_2$** – dried under high vacuum (10^{-5} mbar) contained 2.90 wt% Pt, 1.62 wt% Zn (1.66 equiv. Pt^{-1}), 4.44 wt% C (24.9 equiv. Pt^{-1}) and 0.79 wt% H (52.7 equiv. Pt^{-1}). The too high C and H values (20 C and 39 H expected) can be explained by a chemisorption (coordination) of some of the released $HOSi(OtBu)_3$ – formed during grafting of the Pt precursor – on the silica-support containing Zn^{II} Lewis acid sites. This is evidenced by the low amount of observed $HOSi(OtBu)_3$ released in solution compared to amount of remaining $[Pt(OSi(OtBu)_3)_2(COD)]$, revealing that 45% of the expected $HOSi(OtBu)_3$ is missing and remains chemisorbed at the surface of the support consistent with the elemental analysis. The IR spectrum revealed only partial consumption of the surface OH groups compared to **Zn^{II}/SiO_2**. This process is accompanied by the appearance of ν(C–H) at 3000–2800 cm^{-1} and δ(C–H) at 1500–1340 cm^{-1} (Fig. 1(b) and ESI Fig. S3†). All these data are consistent with grafting of the Pt^{II} precursor through surface OH groups and the retention of some silanol on the surface. Furthermore, solid-state NMR supports the formation of ≡SiOPt$(OSi(OtBu)_3)(COD)$ with signals at 1.5 ppm and 5.0 ppm in ^{1}H SSNMR and signals at 30 ppm and 91 ppm in the ^{13}C SSNMR spectrum, respectively (ESI Fig. S4 and S5†). The data is consistent with the formation of a grafted Pt^{II} complex together with Zn single-sites in **$Pt(OSi(OtBu)_3)(COD)Zn^{II}/SiO_2$**. The material was subsequently treated under H_2 at 600 °C for

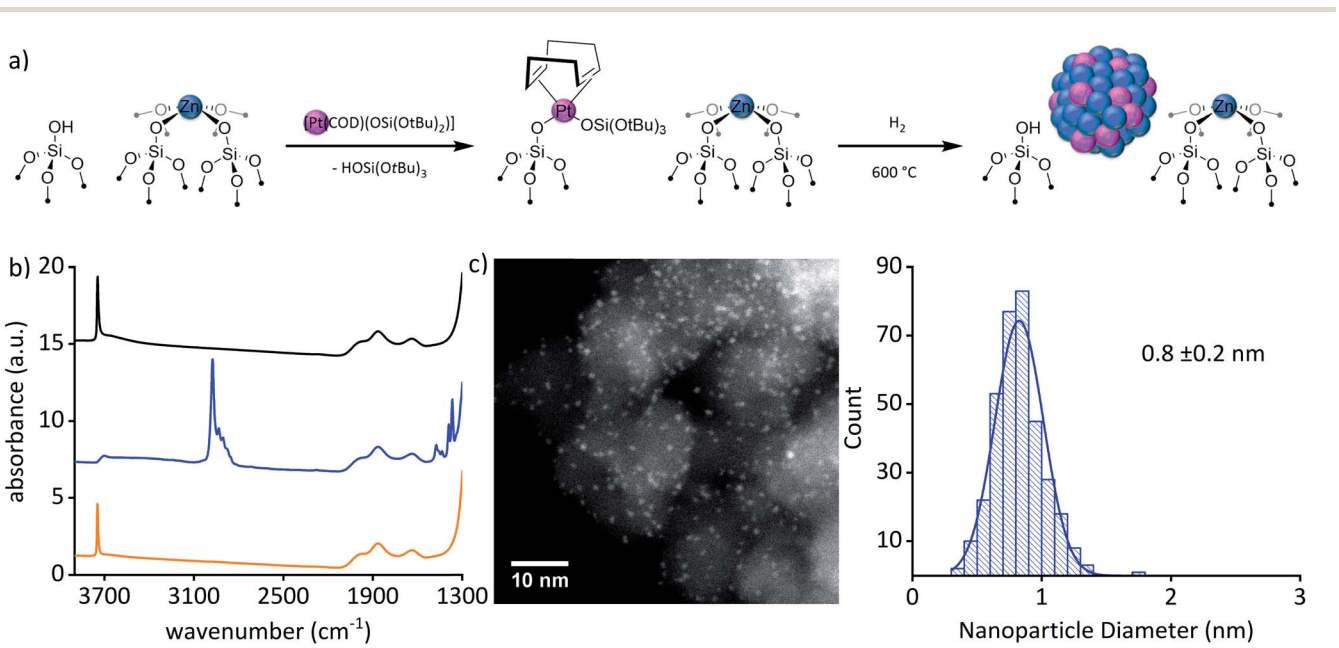

Fig. 1 (a) Schematic representation of the synthesis of the material $Pt^0Zn^{\delta+}/SiO_2$. (b) FTIR spectra of Zn^{II}/SiO_2 (orange), $Pt(OSi(OtBu)_3)(COD)Zn^{II}/SiO_2$ (blue) and $Pt^0Zn^{\delta+}/SiO_2$ (black). (c) Representative HAADF-STEM image and particle size distribution of $Pt^0Zn^{\delta+}/SiO_2$.

8 h yielding a black material – $Pt^0Zn^{\delta+}/SiO_2$ – suggesting the formation of particles (3.05 wt% Pt, 1.54 wt% Zn). HAADF-STEM images of $Pt^0Zn^{\delta+}/SiO_2$ confirmed the formation of well-dispersed and narrowly distributed sub-nanometric particles (0.8 ± 0.2 nm) (Fig. 1(c)).

The IR spectrum of a $Pt^0Zn^{\delta+}/SiO_2$ self-supporting pellet exposed to CO (3 mg, 12 mbar) shows an intense CO vibrational band centered at 2046 cm^{-1} that is red shifted by 38 cm^{-1} compared to what is observed for Pt particles (2084 cm^{-1}) supported on silica – Pt^0/SiO_2 (2.2 ± 0.8 nm) – prepared by a similar approach (grafting of $[Pt(OSi(OtBu)_3)_2(COD)]$ onto SiO_{2-700} followed by a treatment under H_2 at 500 °C). The shift is ascribed to an inherent difference in the particle surfaces of the Pt^0/SiO_2 and $Pt^0Zn^{\delta+}/SiO_2$ materials attributed to alloy formation of the two components in $Pt^0Zn^{\delta+}/SiO_2$ (Fig. 2(a)).[26] Additionally, H_2 and CO chemisorption studies also support the inherent difference of the particle surface in $Pt^0Zn^{\delta+}/SiO_2$ compared to Pt^0/SiO_2 (see ESI† for details). A background subtracted spectrum of $Pt^0Zn^{\delta+}/SiO_2$ (12 mg, 120 mbar CO; Fig. 2(b)) shows weak bands at 2202 cm^{-1} and 2179 cm^{-1} consistent with CO adsorbed on Zn^{II} sites, similar to those found in Zn^{II}/SiO_2 (13 mg, 123 mbar CO; 2206 cm^{-1}) and Zn^{II} sites that are likely to be in close proximity to the alloyed particles. Another band at 1906 cm^{-1} – not observable for Pt^0/SiO_2 – is consistent with a μ_2-binding mode of CO on the $Pt^0Zn^{\delta+}/SiO_2$ material. In addition to the CO IR studies, pyridine desorption was also used to probe the surface property of the material. Vibrational bands at 1538 cm^{-1}, 1438 cm^{-1} and 1408 cm^{-1} are associated with the interaction of pyridine with Pt species on SiO_2 and α-pyridyl species on Pt{111}.[27,28] Bands at 1610 cm^{-1} and 1452 cm^{-1} – similar to Zn^{II}/SiO_2 – as well as 1595 cm^{-1} and 1445 cm^{-1} for $Pt^0Zn^{\delta+}/SiO_2$ indicate two different types of Lewis acidic Zn sites – a stronger and a weaker one – on the surface of the material.[22,29] No bands above 1610 cm^{-1} indicate a low Brønsted acidity of the support (see ESI† for details).[30] The combined results of the CO and pyridine IR studies suggest the formation of an alloyed Pt–Zn material along with residual surface Zn^{II} sites.

XPS was used to gather further insight in the chemical state of Pt and Zn as well as the composition of the material. The results are summed up in Table 1. The Pt $4f_{7/2}$ binding energy in $Pt^0Zn^{\delta+}/SiO_2$ is 71.6 eV which is shifted by +0.3 eV compared to Pt^0/SiO_2, likely due to the restructuring of the Pt 4f states upon alloying with Zn.[31] The Zn $2p_{3/2}$ peak for Zn^{II}/SiO_2 consists of a symmetric component centered at 1023.1 eV (Fig. 2(c)), while the Zn $2p_{3/2}$ peak for $Pt^0Zn^{\delta+}/SiO_2$ (Fig. 2(d)) is asymmetric and was therefore fitted with two components at 1021.7 eV (55% of area) and 1023.1 eV (45% of area). The lower binding energy

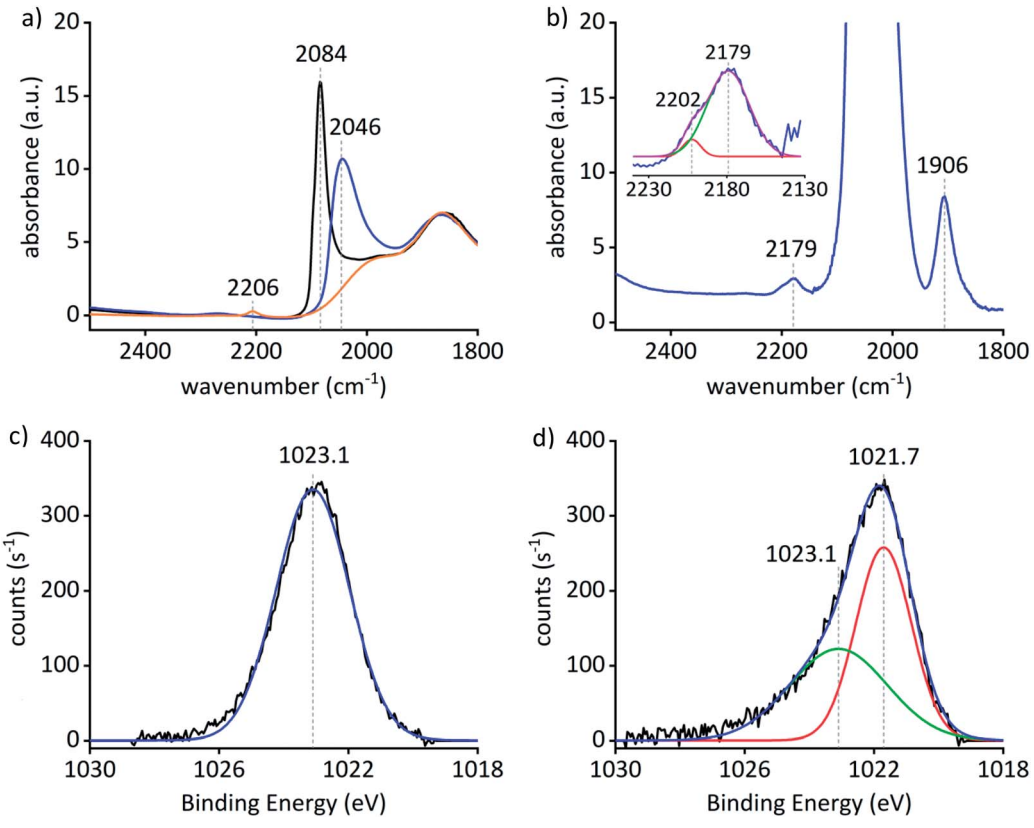

Fig. 2 (a) CO adsorption on Pt^0/SiO_2 (black), Zn^{II}/SiO_2 (orange) and $Pt^0Zn^{\delta+}/SiO_2$ (blue). The spectra are normalized to the υ_{SiO} vibrational frequency at 1865 cm^{-1}. (b) Background subtracted spectrum of CO adsorption on $Pt^0Zn^{\delta+}/SiO_2$ (blue) and two component Gaussian fit (red, green; cumulative fit (purple)) of the CO adsorption region around 2179 cm^{-1} of $Pt^0Zn^{\delta+}/SiO_2$. (c) High resolution Zn $2p_{3/2}$ XPS spectrum of Zn^{II}/SiO_2 (black) and Gaussian–Lorentzian fit to the data (blue). (d) High resolution Zn $2p_{3/2}$ XPS spectrum for $Pt^0Zn^{\delta+}/SiO_2$ (black), two component Gaussian–Lorentzian fit to the data (green: 45%; red: 55%) and cumulative fit (blue).

Table 1 XPS $2p_{3/2}$ and $4f_{7/2}$ data of the Zn^{II}/SiO_2, Pt^0/SiO_2 and $Pt^0Zn^{\delta+}/SiO_2$ materials

Sample	Zn $2p_{3/2}$ BE [eV]	Pt $4f_{7/2}$ BE [eV]	FWHM $2p_{3/2}$ [eV]	FWHM $4f_{7/2}$ [eV]
$\mathbf{Zn^{II}/SiO_2}$	1023.1	—	2.7	—
$\mathbf{Pt^0/SiO_2}$	—	71.3[a]	—	2.1[a]
$\mathbf{Pt^0Zn^{\delta+}/SiO_2}$	1021.7; 1023.1	71.6	2.0; 3.6	2.1

[a] Value taken from ref. 21.

component can be attributed to Zn^0 (through Zn^{II} reduction). This binding energy is close to the reported value for Zn metal (1021.8(2) eV),[32] while the other value parallels what is found for $\mathbf{Zn^{II}/SiO_2}$, in accordance with a minority of Zn remaining on the surface as Zn^{II}.

X-ray absorption studies of the materials have also been performed at the Zn K-edge and Pt L_3-edge in order to obtain a better understanding of the nature of Pt and Zn in the catalyst precursors and $\mathbf{Pt^0Zn^{\delta+}/SiO_2}$. Fig. 3(a) shows the Zn K-edge X-ray absorption near-edge structure (XANES) spectra of $\mathbf{Pt(OSi(O}t\mathbf{Bu)_3)(COD)Zn^{II}/SiO_2}$, $\mathbf{Pt^0Zn^{\delta+}/SiO_2}$ and Zn foil. An edge shift of −3.8 eV from $\mathbf{Pt(OSi(O}t\mathbf{Bu)_3)(COD)Zn^{II}/SiO_2}$ to $\mathbf{Pt^0Zn^{\delta+}/SiO_2}$ clearly indicates the reduction of Zn^{II} to Zn^0. The differences in shape and edge position of $\mathbf{Pt^0Zn^{\delta+}/SiO_2}$ compared to Zn foil are attributed to alloy formation of Zn with Pt along with Zn^{II} species as supported by comparison of the derivative spectra of $\mathbf{Pt(OSi(O}t\mathbf{Bu)_3)(COD)Zn^{II}/SiO_2}$ and $\mathbf{Pt^0Zn^{\delta+}/SiO_2}$ (Fig. 3(b)) revealing the existence of a remaining oxidized Zn species in $\mathbf{Pt^0Zn^{\delta+}/SiO_2}$ – in accordance with the observations of adsorption IR studies and XPS – attributed to Zn^{II} sites on the support surface. A linear combination fit of $\mathbf{Pt(OSi(O}t\mathbf{Bu)_3)(COD)Zn^{II}/SiO_2}$ and Zn foil spectra suggests 22% of Zn remaining as Zn^{II} sites on the surface of $\mathbf{Pt^0Zn^{\delta+}/SiO_2}$ (ESI Fig. S21†). Analysis of the extended X-ray absorption fine structure (EXAFS) of the Zn K-edge of the material precursors $\mathbf{Pt(OSi(O}t\mathbf{Bu)_3)(COD)Zn^{II}/SiO_2}$ and $\mathbf{Zn^{II}/SiO_2}$ (see Table 2 and ESI Fig. S24–S27 and Tables S4, S5†) reveals a significant elongation of the Zn–O bond distance in the former material compared to the latter, an indication for some changes in the local environment of Zn upon grafting of $Pt(OSi(OtBu)_3)_2(COD)$, consistent with the interaction of the Zn^{II} sites with the Pt precursor. In both materials the inclusion of a Zn–Zn instead of a Zn–Si path decreased the fit quality significantly – indicating the high dispersion of Zn^{II} single sites in the precatalyst before the H_2 treatment – also confirmed by a wavelet analysis of $[Zn(OSi(OtBu)_3)_2]_2$ and $\mathbf{Pt(OSi(O}t\mathbf{Bu)_3)(COD)Zn^{II}/SiO_2}$ (ESI Fig. S28–S33†), clearly showing the disappearance of the Zn–Zn scattering pathway in the latter material. Detailed EXAFS analysis of $\mathbf{Pt^0Zn^{\delta+}/SiO_2}$ was not possible due to the presence of overlapping scattering paths, resulting in fits without physical meaning.

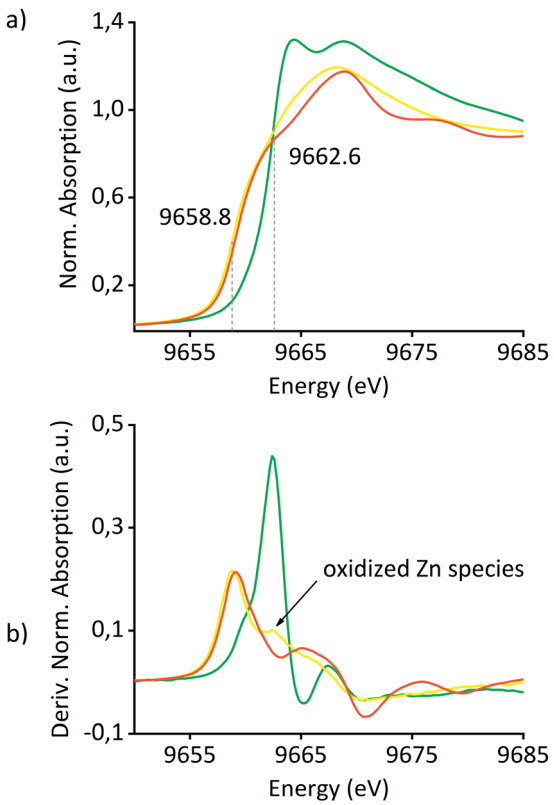

Fig. 3 (a) XANES spectra of $Pt(OSi(OtBu)_3)(COD)Zn^{II}/SiO_2$ (green), $Pt^0Zn^{\delta+}/SiO_2$ (yellow) and Zn foil (red). (b) First derivative spectra of the same materials.

XANES analysis of the Pt L_3 edge of $\mathbf{Pt(OSi(O}t\mathbf{Bu)_3)(COD)Zn^{II}/SiO_2}$ and $\mathbf{Pt^0Zn^{\delta+}/SiO_2}$ follows similar trends as the Zn K edge (ESI Fig. S33 and S34†) with a strong decrease in white line intensity upon H_2 treatment – indicating reduction of the corresponding metal – and a shift to lower edge energy, supporting what was observed for the Zn K edge. EXAFS analysis of the Pt L_3 edge of $\mathbf{Pt^0/SiO_2}$ and $\mathbf{Pt^0Zn^{\delta+}/SiO_2}$ (see Table 2) reveals a considerably shortened Pt–Pt bond distance in the bimetallic material consistent with structural changes and alloy formation. Furthermore, an approximately 2 : 1 (Zn : Pt) ratio of nearest neighbours for $\mathbf{Pt^0Zn^{\delta+}/SiO_2}$ suggests a 1 : 1 metal ratio in the nanoparticles (see ESI† for details). However, large errors on the coordination numbers and the fact that XAS only provides average data do not allow the precise determination of particle composition and homogeneity of the alloying. Based on the EA, XPS and XAS results, it can be concluded that $\mathbf{Pt^0Zn^{\delta+}/SiO_2}$ consists of alloyed, Pt–Zn nanoparticles supported on SiO_2 with a fraction of 0.2 to 0.4 of the total Zn remaining as Zn^{II} sites on the surface of the material.

The materials $\mathbf{Zn^{II}/SiO_2}$, $\mathbf{Pt^0/SiO_2}$ and $\mathbf{Pt^0Zn^{\delta+}/SiO_2}$ were then tested in the PDH reaction at 550 °C under flow conditions

Table 2 EXAFS fit parameters of Pt L_3-edge and Zn K-edge spectra for selected samples[a]

Sample	Neighbor, N[b]	r[c] [Å]	σ^{2d} [Å^2]
	Pt L_3-edge		
$Pt^0Zn^{\delta+}/SiO_2$	Pt, 3.1 ± 1.4	2.62 ± 0.01	0.008 ± 0.002
	Zn, 6.7 ± 2.4	2.48 ± 0.03	0.022 ± 0.004
Pt^0/SiO_2	Pt, 9.1 ± 0.4	2.747 ± 0.002	0.0058 ± 0.0002
	Zn K-edge		
Zn^{II}/SiO_2	O, 3.5 ± 0.9	1.88 ± 0.02	0.016 ± 0.004
	Si, 0.7 ± 0.6	3.07 ± 0.04	0.005 ± 0.008
$Pt(OSi(OtBu)_3)(COD)Zn^{II}/SiO_2$	O, 3.8 ± 0.5	1.94 ± 0.01	0.011 ± 0.002
	Si, 0.7 ± 0.4	3.09 ± 0.02	0.002 ± 0.004

[a] Samples recorded in transmission mode. [b] Number of specified neighbors. [c] Distance to neighbor. [d] Debye–Waller factor.

(50 ml min^{-1}; 20% C_3H_8 in Ar) in a stainless-steel tubular reactor where negligible mass and heat transfer limitations occur (see calculations in ESI†). The results are summarized in Table 3. A very high initial productivity 703 $g_{C_3H_6}$ g_{Pt}^{-1} h^{-1} with a conversion of 30.2% and selectivity of 98.1% to C_3H_6 could be achieved for **$Pt^0Zn^{\delta+}/SiO_2$** at a WHSV of 75 h^{-1}. The high selectivity could be maintained over the course of 30 h time on stream with a final selectivity of 95.0% while the conversion dropped to a final 16.1% conversion (k_d = 0.027 h^{-1} – see eqn (1)) and a productivity of 375 $g_{C_3H_6}$ g_{Pt}^{-1} h^{-1}.

$$k_d = \frac{\left(\ln\left(\frac{1-\mathrm{conv_{end}}}{\mathrm{conv_{end}}}\right) - \ln\left(\frac{1-\mathrm{conv_{start}}}{\mathrm{conv_{start}}}\right)\right)}{t} \quad (1)$$

Catalytic tests at lower WHSV of 32 h^{-1} showed a significant increase in the initial conversion up to 35.3%, while maintaining high selectivity (>96%) and an almost closed carbon balance (97%). In contrast, **Pt^0/SiO_2** shows a very low initial productivity (14.5 $g_{C_3H_6}$ g_{Pt}^{-1} h^{-1}) and a high deactivation rate (k_d = 0.26) over the course of 2 h, while **Zn^{II}/SiO_2** shows comparable catalytic performance to SiO_{2-700} (1.2% conversion, 39–38% selectivity over 10 h) revealing the absence of catalytic activity of **Zn^{II}/SiO_2** under these conditions.

Comparison of **$Pt^0Zn^{\delta+}/SiO_2$** to the monometallic **Pt^0/SiO_2** shows a dramatic improvement in the productivity of the bimetallic system by more than one order of magnitude. Comparison of **$Pt^0Zn^{\delta+}/SiO_2$** to other Pt–Zn systems reveals superior stability of the reported system (ESI Table S9†). While most systems show high selectivity and conversion levels, significantly larger deactivation factors are observed in comparison to **$Pt^0Zn^{\delta+}/SiO_2$** or the studies include H_2 co-feeding[33] and significantly lower weight hourly space velocities to decrease deactivation rates. Furthermore, the metal based productivity and the stability of the reported system also surpass these of the recently published Pt–Ga based system (661 (357 after 20 h) $g_{C_3H_6}$ g_{Pt}^{-1} h^{-1}; k_d = 0.041 h^{-1}) prepared *via* the same SOMC/TMP approach.[21]

To further investigate the structural stability of **$Pt^0Zn^{\delta+}/SiO_2$** under PDH conditions *in situ* XAS studies were performed under the same conditions as the catalytic tests. The spectra of **$Pt^0Zn^{\delta+}/SiO_2$** and **Pt^0/SiO_2** show no significant change at the Pt L_3 edge over 8 h and 2 h, respectively. The Zn K edge spectra of **$Pt^0Zn^{\delta+}/SiO_2$** show a slight and consistent shift over 8 h, indicating a slight structural change for Zn. Preliminary analysis indicates the further – but not complete – reduction of Zn^{II} sites to Zn^0 (ESI Fig. S48 and S49†).

The very high productivity of the reported **$Pt^0Zn^{\delta+}/SiO_2$** system compared to most other Pt–Zn systems is attributed to the formation of subnanometric alloyed particles, probably a result of the high metal dispersion in the precatalyst before reduction. These particles show minor growth during catalysis

Table 3 Catalytic performance of $Pt^0Zn^{\delta+}/SiO_2$, Pt^0/SiO_2 and Zn^{II}/SiO_2 at 550 °C under flow conditions[a]

Sample	Time [h]	Conversion [%]	Selectivity[b] [%]	Carbon balance [%]	Productivity [$g_{C_3H_6}/g_{Pt}^{-1}$ h^{-1}]	WHSV [h^{-1}]	k_d[c] [h^{-1}]
Pt^0/SiO_2	0.1	2.5	74.9	>99	14.5	32	0.26
	2	1.5	47.1		8.7		
Zn^{II}/SiO_2	0.1	0.9	43.3	>99	—	32	0
	10	0.9	39.6		—		
$Pt^0Zn^{\delta+}/SiO_2$	0.1	35.3	97.6	97	350	32	0.014
	30	26.6	96.3		264		
$Pt^0Zn^{\delta+}/SiO_2$	0.1	30.2	98.1	97	703	75	0.027
	30	16.1	95.0		375		

[a] 50 ml min^{-1}, 20% C_3H_8 in Ar. [b] Selectivity for C_3H_6, only volatile compounds taken into account. [c] $kd = (\ln((1 - \mathrm{conv_{end}})/\mathrm{conv_{end}}) - \ln((1 - \mathrm{conv_{start}})/\mathrm{conv_{start}}))/t$.

over 30 h as shown by post-catalysis TEM analysis (ESI Fig. S8†). The narrow particle size distribution and the presence of remaining Lewis acidic Zn^{II} sites on the materials surface could both play a significant role in stabilizing this catalyst. Post-catalysis characterization shows the formation of coke as well as minor particle growth (ESI Fig. S8 and S54†), which both are most likely contributing to catalyst deactivation.

Conclusions

This work shows that utilizing SOMC/TMP as a synthetic methodology enables the formation of narrowly distributed bimetallic Pt–Zn subnanometric particles supported on SiO_2. The resulting high productivity and stability in the PDH reaction for the tested range of WHSV compared to other Pt–Zn systems are attributed to the combination of alloying and high metal dispersion. Furthermore, the remaining Zn^{II} surface sites likely play a role to prevent sintering. SOMC/TMP is a unique synthetic tool to address the origin of catalytic performances in complex multi-metallic systems, where composition, size and support effects can play a crucial role; we are currently further investigating this approach as a general tool for the synthesis of model catalysts to establish detailed structure–activity relationships.

Conflicts of interest

There are no conflicts to declare.

Acknowledgements

L. S. R. thanks the Swiss National Science Foundation (SNSF fond number: 200021_169134) for funding. J. A. thanks the Sinergia project of the Swiss National Science Foundation (SNSF fond number: CRSII5_183495) for funding. We thank Dr Dmitry Lebedev and ScopeM for help with TEM measurements. Fabian Müller and Debora Thöny are acknowledged for help with TGA measurements. Ka Wing Chan is thanked for help with XAS interpretation. Scott Docherty is acknowledged for help with chemisorption measurements. Dr Gina Noh, David Trummer, Petr Šot and Scott Docherty are acknowledged for discussions. The whole Copéret group is acknowledged for help with XAS measurements.

References

1 J. S. Plotkin, *The Propylene Gap: How Can It Be Filled? – American Chemical Society*, https://www.acs.org/content/acs/en/pressroom/cutting-edge-chemistry/the-propylene-gap-how-can-it-be-filled.html, accessed 1 November 2019.
2 J. S. Plotkin, *The Propylene Quandary – American Chemical Society*, https://www.acs.org/content/acs/en/pressroom/cutting-edge-chemistry/the-propylene-quandary.html, accessed 1 November 2019.
3 J. J. H. B. Sattler, J. Ruiz-Martinez, E. Santillan-Jimenez and B. M. Weckhuysen, *Chem. Rev.*, 2014, **114**, 10613–10653.
4 J. Liu, W. Zhou, D. Jiang, W. Wu, C. Miao, Y. Wang and X. Ma, *Ind. Eng. Chem. Res.*, 2018, **57**, 11265–11270.
5 Z. Han, S. Li, F. Jiang, T. Wang, X. Ma and J. Gong, *Nanoscale*, 2014, **6**, 10000–10008.
6 E. C. Wegener, Z. Wu, H.-T. Tseng, J. R. Gallagher, Y. Ren, R. E. Diaz, F. H. Ribeiro and J. T. Miller, *Catal. Today*, 2018, **299**, 146–153.
7 J. J. H. B. Sattler, I. D. Gonzalez-Jimenez, L. Luo, B. A. Stears, A. Malek, D. G. Barton, B. A. Kilos, M. P. Kaminsky, T. W. G. M. Verhoeven, E. J. Koers, M. Baldus and B. M. Weckhuysen, *Angew. Chem., Int. Ed.*, 2014, **53**, 9251–9256.
8 Q. Zhang, K. Zhang, S. Zhang, Q. Liu, L. Chen, X. Li, C. Wang and L. Ma, *J. Catal.*, 2018, **368**, 79–88.
9 J. T. Miller, V. J. Cybulskis, B. C. Bukowski, H.-T. Tseng, J. R. Gallagher, Z. Wu, E. Wegener, A. J. Kropf, B. Ravel, F. H. Ribeiro and J. Greeley, *ACS Catal.*, 2017, **7**, 4173–4181.
10 Z. Nawaz, *Rev. Chem. Eng.*, 2015, **31**, 413–436.
11 Y. Zhang, Y. Zhou, L. Huang, S. Zhou, X. Sheng, Q. Wang and C. Zhang, *Chem. Eng. J.*, 2015, **270**, 352–361.
12 G. Liu, L. Zeng, Z.-J. Zhao, H. Tian, T. Wu and J. Gong, *ACS Catal.*, 2016, **6**, 2158–2162.
13 C. Copéret, A. Comas-Vives, M. P. Conley, D. P. Estes, A. Fedorov, V. Mougel, H. Nagae, F. Núñez-Zarur and P. A. Zhizhko, *Chem. Rev.*, 2016, **116**, 323–421.
14 M. K. Samantaray, E. Pump, A. Bendjeriou-Sedjerari, V. D'Elia, J. D. A. Pelletier, M. Guidotti, R. Psaro and J.-M. Basset, *Chem. Soc. Rev.*, 2018, **47**, 8403–8437.
15 M. M. Stalzer, M. Delferro and T. J. Marks, *Catal. Lett.*, 2015, **145**, 3–14.
16 K. L. Fujdala and T. D. Tilley, *J. Catal.*, 2003, **216**, 265–275.
17 C. Copéret, *Acc. Chem. Res.*, 2019, **52**, 1697–1708.
18 K. Larmier, W.-C. Liao, S. Tada, E. Lam, R. Verel, A. Bansode, A. Urakawa, A. Comas-Vives and C. Copéret, *Angew. Chem., Int. Ed.*, 2017, **56**, 2318–2323.
19 E. Lam, K. Larmier, P. Wolf, S. Tada, O. V. Safonova and C. Copéret, *J. Am. Chem. Soc.*, 2018, **140**, 10530–10535.
20 G. Noh, E. Lam, J. L. Alfke, K. Larmier, K. Searles, P. Wolf and C. Copéret, *ChemSusChem*, 2019, **12**, 968–972.
21 K. Searles, K. W. Chan, J. A. Mendes Burak, D. Zemlyanov, O. Safonova and C. Copéret, *J. Am. Chem. Soc.*, 2018, **140**, 11674–11679.
22 A. K. Cook and C. Copéret, *Organometallics*, 2018, **37**, 1342–1345.
23 N. Rendón, A. Bourdolle, P. L. Baldeck, H. Le Bozec, C. Andraud, S. Brasselet, C. Coperet and O. Maury, *Chem. Mater.*, 2011, **23**, 3228–3236.
24 P. Laurent, L. Veyre, C. Thieuleux, S. Donet and C. Copéret, *Dalton Trans.*, 2013, **42**, 238–248.
25 D. A. Ruddy, J. Jarupatrakorn, R. M. Rioux, J. T. Miller, M. J. McMurdo, J. L. McBee, K. A. Tupper and T. D. Tilley, *Chem. Mater.*, 2008, **20**, 6517–6527.
26 A. G. T. M. Bastein, F. J. C. M. Toolenaar and V. Ponec, *J. Catal.*, 1984, **90**, 88–95.
27 B. A. Morrow, I. A. Cody, L. E. Moran and R. Palepu, *J. Catal.*, 1976, **44**, 467–476.

28 S. Haq and D. A. King, *J. Phys. Chem.*, 1996, **100**, 16957–16965.
29 C. Morterra and G. Cerrato, *Catal. Lett.*, 1991, **10**, 357–363.
30 R. Ferwerda, J. H. van der Maas and F. B. van Duijneveldt, *J. Mol. Catal. A: Chem.*, 1996, **104**, 319–328.
31 J. A. Rodriguez and M. Kuhn, *J. Chem. Phys.*, 1995, **102**, 4279–4289.
32 S. P. Kowalczyk, R. A. Pollak, F. R. McFeely, L. Ley and D. A. Shirley, *Phys. Rev. B: Solid State*, 1973, **8**, 2387–2391.
33 V. Galvita, G. Siddiqi, P. Sun and A. T. Bell, *J. Catal.*, 2010, **271**, 209–219.